REMOTE QUANTIFICATION OF SMOKESTACK TOTAL EFFLUENT MASS FLOW RATES USING IMAGING FOURIER-TRANSFORM SPECTROSCOPY

THESIS

Jacob Harley, Captain, USAF

AFIT/GE/ENP/11-M01

DEPARTMENT OF THE AIR FORCE
AIR UNIVERSITY

AIR FORCE INSTITUTE OF TECHNOLOGY

Wright-Patterson Air Force Base, Ohio

AFIT/GE/ENP/11-M01

REMOTE QUANTIFICATION OF

SMOKESTACK TOTAL EFFLUENT MASS FLOW RATES

USING IMAGING FOURIER-TRANSFORM SPECTROSCOPY

THESIS

Presented to the Faculty

Department of Electrical and Computer Engineering

Graduate School of Engineering and Management

Air Force Institute of Technology

Air University

Air Education and Training Command

in Partial Fulfillment of the Requirements for the

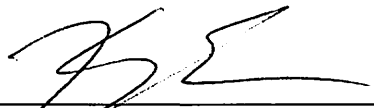Degree of Master of Science in Physics

Jacob Harley, BS

Captain, USAF

March 2011

REMOTE QUANTIFICATION OF

SMOKESTACK TOTAL EFFLUENT MASS FLOW RATES

USING IMAGING FOURIER-TRANSFORM SPECTROSCOPY

Jacob Harley, BS
Captain, USAF
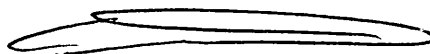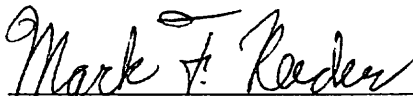
Approved:

_____
Kevin C. Gross, PhD (Chairman)

_____
4 -Mar-2011
Date

_____
Glen P. Perram, PhD (Member)

_____
4 MAR 11
Date

_____
Mark F. Reeder, PhD (Member)

_____
4 Mar 11
Date

Abstract

A Telops Hyper-Cam midwave infrared $(1.5-5.5\,\mu m)$ imaging Fourier-transform spectrometer (IFTS) was used to estimate industrial smokestack total effluent mass flow rates by combining spectrally-determined species concentrations with flow rates estimated via analysis of sequential images in the raw interferogram cube. Measurements of the coal-burning smokestack were made with the IFTS at a stand-off distance of $350\,m$. 185 hyperspectral datacubes were collected on a $128\,(W) \times 64\,(H)$ pixel sub-window $(11.4 \times 11.4\,cm^2$ per pixel) at a $0.5\,cm^{-1}$ spectral resolution. Strong emissions from H_2O, CO_2, CO, SO_2, and NO were observed in the spectrum. A previously established single-layer radiative transfer model was used to estimate gas concentrations immediately above stack exit, and results compared reasonably with *in situ* measurements. A simple temporal cross-correlation analysis of sequential imagery enabled an estimation of the flow velocity at center stack. The estimated volumetric flow rate of $106 \pm 23\,\mathrm{m/s}$ was within 4% of the reported value. Final effluent mass flow rates for CO_2 and SO_2 of $13.5 \pm 3.78\,\mathrm{kg/s}$ and $71.3 \pm 19.3\,\mathrm{g/s}$ were in good agreement with *in situ* rates of $11.6 \pm 0.07\,\mathrm{kg/s}$ and $67.8 \pm 0.52\,\mathrm{g/s}$. NO was estimated at $16.1 \pm 4.19\,\mathrm{g/s}$, which did not compare well to the total NO_x $(NO + NO_2)$ reported value of $11.2 \pm 0.16\,\mathrm{g/s}$. Unmonitored H_2O, HCl, and CO were also estimated at $7.76 \pm 2.25\,\mathrm{kg/s}$, $7.40 \pm 2.00\,\mathrm{g/s}$, and $15.0 \pm 4.05\,\mathrm{g/s}$ respectively.

Acknowledgements

I would like to thank my family for their constant support throughout this process. My wife has been invaluable, and I would have been completely lost without her. My daughter's patience has allowed me to feel like a good father even while I mostly stressed out and barely retained focus. My two year old son could not have cared less about my stress, and his ability to scream my name and run at me the moment I walked through the door proved to be consistently medicinal.

The AFIT experience has been fantastic and the staff has made it so. My thesis advisor, Dr. Gross, maintained a level of energy and interest in my work which baffled me at times. His ability to help me refocus was vital, and he pulled me from the academic brink more times than probably should have been necessary. He is completely commited to his work and his students. I wish him the best of luck in the future, and I hope this thesis does not disappoint.

Jacob Harley

Table of Contents

List of Figures

List of Tables

List of Abbreviations

REMOTE QUANTIFICATION OF

SMOKESTACK TOTAL EFFLUENT MASS FLOW RATES

USING IMAGING FOURIER-TRANSFORM SPECTROSCOPY

I. Introduction

The passive optical remote sensing of chemical plumes is a well established field, and Fourier-transform spectroscopic (FTS) techniques, specifically, have been thoroughly developed. However, with the advent of imaging Fourier-transform spectroscopy (IFTS), the traditional capabilities of FTS are greatly enhanced and some limitations are eliminated. Measuring species concentrations solely using FTS can be complicated due to the technique's spatial limitations. These complications can be removed with an IFTS. With an interferogram captured at every pixel on a focal plane array (FPA) it is possible to reduce concerns of inhomogeneity caused by spatial averaging, and the broadened field of view (FOV) ensures the desired region of the plume is measured [9, 31]. The work done by Gross *et al.* showed the impact imagery can have on concentration estimation. In that work, using only the Telops Hyper-Cam (a highly capable IFTS), fractional column densities were estimated using a single-layer radiative transfer model. The success of that effort led to an understanding of the potential unlocked by leveraging the time-resolved direct current (DC) level imagery. The scope of this work is to extend the exploitation of the imagery and merge flow field analysis with the already successful concentration estimation technique to determine a final effluent mass flow rate. A method of tracking brightness features across pixels through a measured number of frames to determine a flow velocity is developed. With imagery providing an estimation of stack exit diameter,

the two are merged to provide a volumetric flow rate. The ability to remotely verify chemical plumes through optical methods is a mature field and fills an important role in the monitoring of industrial facilities. These methods can be used by oversight agencies to verify reported emissions, and with the increasing portability of the technology this technique could eventually be applied to examine plumes of interest to the Department of Defense.

Research approach

As described above, the ultimate goal of this work is to estimate mass flow rates of individual pollutant species emanating from an industrial smokestack. This task requires both concentration values and a volumetric flow rate. With the method for concentration estimation well in hand the primary focus becomes that of flow field analysis. An important subset of the goal is to accomplish this feat using only the data captured by the Telops Hyper-Cam during a single, short deployment. The volumetric flow rate is primarily dependent on an estimation of the upward flow velocity of the plume, as the ability to estimate plume cross-section from imagery has already been proven. Prior to deployment for smokestack data acquisition, the Telops was used to examine a thermal plume generated by a heated laboratory blower. The results of the velocity estimation using the brightness feature tracking method were in excellent agreement with the measured values, and a computational method needed to be developed to examine the large-scale smokestack data. The method developed is relatively unsophisticated and is no doubt influenced by the complications inherent in observing a turbulent plume in a crosswind. A more sophisticated model is possible and recommended for future work, however this work is intended as a proof-of-concept and a way forward using the technique.

Document structure

Chapter II of this document presents a review of research critical to this work. Various remote sensing techniques are examined, with an emphasis on passive remote sensing, and several applicable flow estimation techniques are discussed. An investigation of some research in the fields of fluid dynamics and turbulent plumes is also presented, which was vital to flow analysis and influenced the region selected for accurate velocity estimation. Chapter III presents an article on the subject of remote quantification of smokestack total effluent mass flow rates using IFTS. The paper has been accepted for oral presentation at the Chemical, Biological, Radiological, Nuclear, and Explosives (CBRNE) Sensing XII conference. While there is some content overlap with the first two chapters of this thesis, the paper is presented in its entirety and contains the experimental description, underlying theory, final estimation results, and conclusions that are the core of this work. Appendix A is an expanded discussion of the velocity estimation work. The theory and results presented in Chapter III are concise, and additional discussion of some of the underlying plume behavior and velocities seemed warranted. The Reynolds number and Morton length equations and calculations are given in Appendix B. Lastly, Appendix C contains MATLAB code developed specifically for the brightness feature tracking method and plume flow analysis. Each primary section of code is introduced with an overarching description of its purpose, and line specific comments are included where applicable.

II. Literature Review

Both active and passive remote sensing techniques have been successfully applied toward the estimation of chemical concentrations in plumes. Both active and passive methods were reviewed below, with an emphasis on passive techniques due to the nature of the Telops Hyper-Cam. Specifically, Fourier-transform spectroscopy and the efforts taken by Gross *et al.* in the previous Telops effluent concentration estimation work were the primary focus of the remote sensing review. A multitude of flow velocity estimation techniques are available. Plume behavior has been remotely analyzed and flow velocity has been successfully characterized through several proven methods such as particle imaging velocimetry (PIV), wind videography, maximum cross-correlation (MCC), and optical flow [32, 10, 21, 3, 17]. The basic tenets of spatial and temporal analysis woven into these various methods led to the model for velocity estimation developed in Chapter III. The complicated nature of thermal plumes and turbulence are important to consider in the selection of an appropriate optical flow estimation technique, and the region of the plume chosen for analysis was a direct result of the research in this area. Therefore, the chapter closes with a review of several key documents used for flow and turbulence understanding in this work.

Remote sensing techniques

Active remote sensing concentration estimation techniques such as lidar have been successfully employed to accurately estimate plume concentrations. Weibring *et al.* remotely applied a differential absorption lidar technique and achieved an accuracy to within ten percent of known values. The mobile lidar system was truck mounted and positioned at several locations during data capture [32]. By interrogating species using a laser tuned to a narrow band these active methods are typically limited to estimating

a small number of species at any one time, but due to the energy provided by the laser, concentrations which would be otherwise too small to detect can be identified. These systems are generally not confined to a single piece of detection equipment and can be more costly in terms of both time and money [9, 32]. In addition to active remote sensing, chemical plume temperatures and species concentrations have long been classified via passive sensing. Wormhoudt describes experiments as early as 1967 which used only a rapid scanning Michelson interferometer to measure an emission spectrum, and the presence of SO_2 was readily detected. In the following years, as instrument resolution and capability increased, additional emission bands were detected, and CO_2, CO, SO_2 and NO were readily seen in the spectra [31]. Due to its measurement across a wide spectrum, multiple species can be detected using only the FTS, and when coupled with temperature can produce concentration estimations [9]. As mentioned in Chapter I, FTS does have limitations in regard to FOV. By introducing a FPA with interferograms at each pixel, IFTS significantly reduces those limitations and makes accurate concentration estimation using a single instrument possible. In 2008, Gross *et al.* successfully estimated effluent concentrations and temperature of an industrial smokestack plume using the Telops Hyper-Cam and a simple single-layer radiative transfer model. This single-layer model assumption was checked by examination of the variation in column density and temperature with location throughout the plume, a check made possible through the spatial resolution provided by the individual interferograms found at each pixel on the FPA. Estimated CO_2 and SO_2 volume fractions of $8.6\pm0.4\,\%$ and $380\pm23\,ppm_v$, respectively, compared favorably with *in situ* measurements of $9.40\pm0.03\,\%$ and $383\pm2\,ppm_v$ [9]. The work done in this thesis relies heavily on the methods and background introduced in the work by Gross *et al.*. The method for concentration estimation was proven feasible and is used to estimate concentrations in the current dataset.

Flow estimation techniques

Flow estimation techniques range from the basic idea of manual object or feature tracking over time steps to the more automated and computational methods. Most rely primarily on high spatial resolution and do not have an extremely refined temporal resolution. PIV and videography have both been used to successfully classify plume flows by spatially tracking unique features or objects through successive images. PIV relies on a seeding of the flow and spatially tracks seed particle movement, and videography measures the displacement of plume structure between camera snapshots [21, 10, 32]. Optical flow methods have been applied to two-dimensional velocity estimation in areas such as sea surface and cloud motion, but this approach is founded on the assumption that the brightness of a feature being tracked will be constant from starting point to ending point [27, 3]. In this work, the turbulent nature of the plume upon stack exit causes a great deal of mixing and temperature fluctuations, which prevents the constant brightness assumption from being satisfied. The MCC technique has been used to detect translational motion in two-dimensional time-sequential satellite images. As with many of the velocity analysis methods, MCC typically leverages well resolved spatial imagery and is not dependent on high temporal resolution [17, 16]. The method of cross-correlation has been extended to this work; however, it is not a spatial correlation between temporally sequential images, but a temporal correlation between spatially sequential pixels in the flow. The temporal axis of the Telops data is extremely resolved due to the kHz framerate, while the spatial resolution is only moderate, therefore it is more beneficial to leverage a method which takes advantage of the temporal strengths within the data. In their treatment of obtaining fluid flow rates through black smoker vents using Optical Plume Velocimetry (OPV), Crone *et al.* evaluate three different methods for estimating the image-velocity field. They found the temporal cross-correlation method produced excellent image-velocity

results and was the most computationally efficient technique. It should be noted they did not recommend this technique for the region of transitional flow, but the camera used in the work was only at $33\,Hz$, which may have impacted capability [13]. In their examination of the Gulf of Mexico oil leak, Crone and Tolstoy use the same OPV method to estimate the flow rate of the oil out of the Deepwater Horizon well. Analysis was focused on flow near the nozzle to allow differences between image velocity and average flow rate at the nozzle to be accounted for with a "shear layer" correction factor. It was then possible to use the median image velocity to determine flow rate. This study used video with a $30\,Hz$ framerate and a $3.85\,\text{pixels/cm}$ spatial resolution [14]. The methods employed by Crone *et al.* lend themselves well to the Telops data, and the flow estimation technique used in this work is very similar.

Thermal plume flow and turbulence

The nature of the smokestack studied in this work can be more understood through calculation of the Reynolds number and the Morton length. According to Blackadar, the Reynolds number is fundamental to the determination of turbulence and is related to the dimensions of the pipe, the flow velocity, and viscosity of the fluid. A flow is typically considered turbulent with a Reynolds number on the order of 1000 or greater. The Reynolds number corresponding to this plume is on the order of 10^6, clearly indicating a turbulent flow [7]. Crone *et al.* describe the Morton length as a relationship between the momentum and buoyancy fluxes which characterizes the regions of jet-like and plume-like flow. When the flow is within one Morton length of stack exit it is considered jet-like and it is considered plume-like at approximately five times the Morton length. Between those two distances the flow is considered transitional [13, 25]. The Morton length for this plume is approximately $2.6\,m$ $(23\,pixels)$, so a small initial region of the analyzed flow field is considered jet-like, while the

remaining plume within the FPA window is in the transitional region. The stack is also influenced by a crosswind at exit, which further impacts turbulence and velocity. Andreopoulos and Rodi investigated jets in a crossflow at several jet-to-crossflow velocity ratios. While the experimental conditions were not the same as those found in this work, due to the careful description of crossflow effects the results are still worthy of consideration. Andreopoulos and Rodi reported on a temperature controlled jet issuing from a circular wall outlet into a cross-stream flowing parallel to the wall. Remaining on central axis above exit, velocity tended to drop as distance from the source increased. While upward velocity would be expected to decay even without a crosswind, these results showed an obvious vertical velocity drop as the motion was completely translated from vertical to horizontal and eventually stabalized to the mean horizontal velocity of the crossflow. In addition, the crossflow in some cases acted like a partial cover over the exit, this caused the jet to bend and initially accelerate on the leeward side while displaying some downwash on the windward side [4]. In his study of the flow structure of the free round turbulent jet in the initial region, Boguslawski presented radial and axial distributions of mean velocities. This turbulent jet was measured in still air and also demonstrated a decay in velocity both with distance from source (as expected and in agreement with the results discussed above) and radially off center axis [8].

III. Remote Quantification of Smokestack Total Effluent Mass Flow Rates Using Imaging Fourier Transform Spectroscopy

Abstract

A Telops Hyper-Cam midwave infrared $(1.5 - 5.5\,\mu m)$ imaging Fourier-transform spectrometer (IFTS) was used to estimate industrial smokestack total effluent mass flow rates by combining spectrally-determined species concentrations with flow rates estimated via analysis of sequential images in the raw interferogram cube. Measurements of the coal-burning smokestack were made with the IFTS at a stand-off distance of $350\,m$. 185 hyperspectral datacubes were collected on a $128\,(W) \times 64\,(H)$ pixel sub-window ($11.4 \times 11.4\,cm^2$ per pixel) at a $0.5\,cm^{-1}$ spectral resolution. Strong emissions from H_2O, CO_2, CO, SO_2, and NO were observed in the spectrum. A previously established single-layer radiative transfer model was used to estimate gas concentrations immediately above stack exit, and results compared reasonably with *in situ* measurements. A simple temporal cross-correlation analysis of sequential imagery enabled an estimation of the flow velocity at center stack. The estimated volumetric flow rate of $106 \pm 23\,\mathrm{m/s}$ was within 4% of the reported value. Final effluent mass flow rates for CO_2 and SO_2 of $13.5 \pm 3.78\,\mathrm{kg/s}$ and $71.3 \pm 19.3\,\mathrm{g/s}$ were in good agreement with *in situ* rates of $11.6 \pm 0.07\,\mathrm{kg/s}$ and $67.8 \pm 0.52\,\mathrm{g/s}$. NO was estimated at $16.1 \pm 4.19\,\mathrm{g/s}$, which did not compare well to the total NO_x $(NO + NO_2)$ reported value of $11.2 \pm 0.16\,\mathrm{g/s}$. Unmonitored H_2O, HCl, and CO were also estimated at $7.76 \pm 2.25\,\mathrm{kg/s}$, $7.40 \pm 2.00\,\mathrm{g/s}$, and $15.0 \pm 4.05\,\mathrm{g/s}$ respectively.

Introduction

The ability to remotely monitor chemical plumes through optical methods is a mature field and fills an important role in the monitoring of industrial facilities. These methods can be used by oversight agencies to verify reported emissions. Estimating temperature and species concentrations through both passive and active remote sensing has long been an option, but quantification of the species is not truly the desired end measurement. An estimation of the total effluent mass flow rates is the ultimate goal. The ability to remotely detect those rates with no *a priori* data using a single measurement tool would be a technical leap from the roots of temperature and species quantification. The imaging capability of the Telops Hyper-Cam IFTS has already been shown to sufficiently bolster the traditional capability of FTS for remote measurement. Temperature and species concentrations of an industrial smokestack plume have been successfully estimated using only the IFTS, proving the combination of both the spatial and spectral capabilities of the tool to be extremely powerful [9]. By leveraging the IR imagery provided by the camera, the door was opened to a host of other possibilities. The same imagery which bolstered the ability to determine concentrations could also be used to gain information about the flow field. Using the Telops Hyper-Cam to determine both pollutant concentrations and a volumetric plume flow rate would allow calculation of the total effluent mass flow rate. The scope of this work is to estimate the mass flow rate of an industrial plume using only the data collected in a single deployment of the Telops Hyper-Cam. This effort focuses on demonstrating a method of measuring volumetric flow while using the previously published concentration estimation model. The ability to remotely verify annual pollution emission rates using a single, easily deployed sensor is highly desirable and is now shown to be possible with an IFTS.

Smokestack effluents have long been identified through various active and passive

means. Active remote sensing concentration estimation techniques such as lidar have been successfully employed to accurately estimate plume concentrations. By interrogating species using a laser tuned to a narrow band these methods are typically limited to estimating a small number of species at any one time. But, due to the energy provided by the laser, concentrations which would be otherwise too small to detect can be identified. These systems are generally not confined to a single piece of detection equipment and can be more costly in terms of both time and money [9, 32]. In addition to active remote sensing, chemical plume temperatures and species concentrations have long been classified via passive sensing. Due to its measurement across a wide spectrum, multiple species can be detected using only the FTS. However, measuring species concentrations solely using FTS can be complicated due to the technique's spatial limitations. These complications are reduced with an IFTS. With an interferogram captured at every pixel on the FPA it is possible to reduce concerns of inhomogeneity caused by spatial averaging, and the broadened FOV ensures the desired region of the plume is measured [9, 31]. The Telops Hyper-Cam IFTS is based on a traditional Michelson interferometer and features a 320×256, 16-bit $(0 - 65,535$ counts$)$ InSb FPA, and each pixel has a $0.326\,mrad$ angular FOV. Modulated intensity images corresponding to successive optical pathlength differences (OPD) are collected on the FPA forming an interferogram cube (i.e., an interferogram at each pixel). In 2008, Gross *et al.* successfully estimated effluent concentrations and temperature of an industrial smokestack plume using the Telops Hyper-Cam and a simple single-layer radiative transfer model. This single-layer model assumption was checked by examination of the variation in column density and temperature with location throughout the plume, a check made possible through the spatial advantages provided by the individual interferograms found at each pixel on the FPA. The narrow FOV at any given pixel minimized the effects of any spatial averaging, while the

11

broad FOV of the entire array provided a complete image of the plume, stack and background. In addition, because it was possible to simultaneously grab both plume and background radiation, only a single data capture session was required. The final spectrally derived concentration estimations of CO_2 and SO_2 agreed to within 9% and 1% respectively with reported values [9]. Due to the experimental overlap, this same simple radiative transfer model from the 2008 Gross experiment is applied to the data captured in this work.

With a proven method for determining effluent concentrations using the data from a Telops Hyper-Cam, the scope of this work is turned to demonstrating a method of volumetric flow estimation from the same data. Flow estimation techniques range from the basic idea of manual object or feature tracking over time steps to the more automated and computational methods. Most rely primarily on high spatial resolution and do not have an extremely refined temporal resolution. Regardless of the method applied in determining the flow field velocity, two specific pieces of information are required to make the determination: the displacement of an object or image and a reliably time-stamped record of that displacement. An IFTS can fulfill both of those requirements. Imagery of the plume's structure captured on the FPA can track the displacement, while the individual images are modulated along set frames providing a known time interval. PIV and videography have been used to successfully classify plume flows in the past [21, 10, 32], and two-dimensional flow fields such as clouds and sea surfaces have been well classified by MCC and optical flow techniques [17, 3]. Optical flow is typically dependent on pixel brightness fluctuations and not on feature locations, and the spatial and time derivatives of image objects are used to establish velocity estimates in both dimensions of the image [3]. The MCC technique has been used to detect translational motion in two-dimensional time-sequential satellite images. This method relies on the cross-correlation between

subsequent images. It tracks features based on the position of the maximum cross-correlation coefficient from subareas of one image to the corresponding neighboring subareas within a designated search window [17, 16]. The idea of cross-correlation to determine velocity certainly influenced this work [32, 16, 17], but in contrast to the spatial correlation techniques described above, the technique presented in this work concentrates on temporal correlation along the image frame axis between spatially sequential pixels. In their development of an OPV technique for examination of seafloor black smokers, Crone *et al.* found a temporal cross-correlation method produced excellent image-velocity results and was the most computationally efficient technique [13, 14].

Estimating a three-dimensional flow from two-dimensional imagery has its complications, and the method proposed below is intended to provide a solution which demonstrates a capability while not becoming too computationally costly. Research regarding flow fields and turbulence has been conducted, and aspects of that research have been applied to this work where applicable and possible. The field of jet and plume characterization is most mature when examining the developed region of the flow and some understanding of velocity and turbulence exists [23, 22, 18, 19, 5]. In attempting to combine flow estimations with effluent concentrations to determine a mass flow rate, this work forces inspection of the plume near stack exit. This area presents some unique problems when attempting to estimate a flow velocity using a temporal cross-correlation method which is dependent on brightness fluctuations. As described in the theory section below, certain assumptions and simplifications are made about regions of the flow in this research in order to support the development of a manageable method and to demonstrate the viability of IFTS as a flow rate characterization option.

Experimental

Instrument description.

As described above, the Telops Hyper-Cam is based on a traditional Michelson interferometer with an InSb FPA, and each pixel's angular FOV which translates to a known spatial distance at the target. Interferograms are captured at each pixel, and a broadband image is captured at each OPD. A complete datacube can be thought of as a single spectral 2D image of the plume generated by the Fourier-transform of the individual interferograms at each pixel, or it can be considered a highly resolved temporal collection of 2D IR images which have been captured at subsequent OPD looking through a Michelson interferometer. The action of the Michelson produces high-frequency modulation coupled with the DC component which can be decoupled to reveal information about the turbulent flow. The full 320×256 pixel set of the array can be windowed to enable faster acquisition rates, although this is done at the expense of reduced spatial resolution. The spectral range covers 1800–$6667\,cm^{-1}$ (1.5–$5.5\,\mu m$), and the spectral resolution can be selected anywhere within the 0.25–$150\,cm^{-1}$ range [9, 11, 15]. The Telops is mounted to a Quickset Gimbal mount with pan and tilt upon a Gibraltar rugged, field deployable tripod to ensure image stability during data capture.

Remote measurements.

The Telops Hyper-Cam was situated approximately $350\,m$ line of sight (LOS) from the top of an industrial smokestack near Dayton, Ohio on an evening in late August; the distance from camera to stack was measured using a Newcon Optik LRB 3000 Pro laser range finder. A schematic detailing the experimental set-up is provided in Figure 1. The coal-burning stack was running at maximum capacity for the duration of the intermittent 45 minute data capture, which began at approximately 0030 hrs
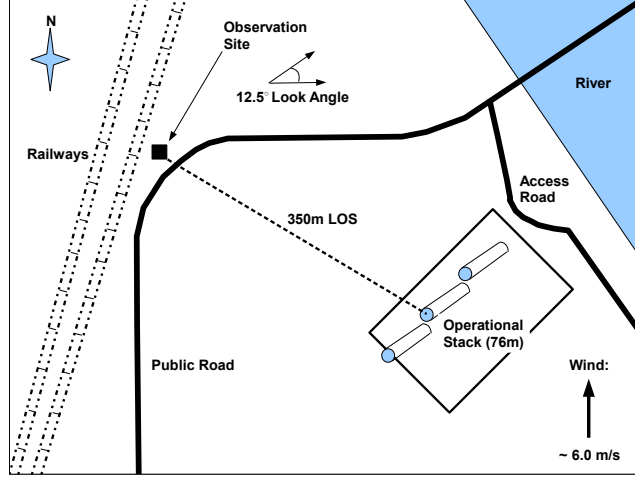
Figure 1. Rendering of experimental setup. The Telops camera was approximately 2 meters off the ground on a Gimbal mount upon a stable tripod. The top of the stack was located 350 meters away from the face of the camera; the camera was pointed at the stack, windowed to a $128\,(W) \times 64\,(H)$ array and locked in place. The average wind speed at stack exit was approximately $6.0\,\text{m/s}$ from the south throughout the collection period.

GMT. A Kestrel 4500 NV Weather Meter was used to capture ambient temperature, pressure, and humidity at the camera, and the sky was uniformly cloudy for the entirety of the data capture window. Average wind speed was from the south and determined by a nearby ($\sim 6\,km$) suburban airport weather station to be roughly $3.6\,\text{m/s}$ at $10\,m$, which translates to approximately $6\,\text{m/s}$ at the $76\,m$ stack exit altitude [1, 6]. At the start of initial data capture a local temperature of $26.2°C$, pressure of $990.5\,hPa$, and humidity of $63.4\,\%$ were found. At the start of the second capture at 0048 hrs GMT, the local temperature was $25.3°C$, the pressure was $991.0\,hPa$, and the humidity was $67.6\,\%$. Two separate capture sessions were required due to problems with some of the acquired datacubes during the initial session. The camera was reset when the problem was noticed, and capture immediately resumed. The coordinates of the Hyper-Cam's capture location were found using two GPS enabled phones, and the location of the smokestack was confirmed using Google Earth imagery.

Radiometric calibration to radiance units $[W/(cm^2 \times sr \times cm^{-1})]$ was accomplished

using two on-board blackbodies set at $45°C$ and $30°C$; calibration occurred prior to measurements. More than 200+ datacubes were recorded, however only 185 were usable due to an intermittent problem with the data acquisition system.

The camera was windowed to 64×128 pixels just above the stack, which ensured focus on stack exit velocity while still granting access to background data to the right of plume. In addition, the reduced pixel count granted an increase in image capture rate. An integration time of $90 \, \mu s$ and spectral resolution of $0.5 \, cm^{-1}$ were used in acquisition, providing an estimated camera framerate of $5 \, kHz$. This framerate was considered ideal to support the pixel to pixel velocity analysis at stack exit.

In situ measurements.

The facility monitored is a $360 \, MW$ coal burning facility built in the late 1940s and is currently operated only under peak power demand. Continuous emissions monitoring is performed, and statistics over the entire data capture timeline were provided. SO_2, NO_x $(NO + NO_2)$, and CO_2 emissions are continuously monitored by three gas monitors. Each is calibrated daily and operates with a precision better than 1%. A wideband LED $(400 - 700 \, nm)$ measures the fraction of attenuated light to quantify plume opacity due to particulate material. A gas flow monitor is located approximately $24 \, m$ below stack exit to track flue gas flow rate and temperature. As a result, estimated temperature at stack exit may be slightly lower than this reported value, but estimated flow rate is expected to be similar. The stack has a measured exit diameter of $4.24 \, m$ and corresponding cross-sectional area of $14.1 \, m^2$ [9]. The inner stack is not tapered, and the same cross-sectional area is found at the monitor point.

16
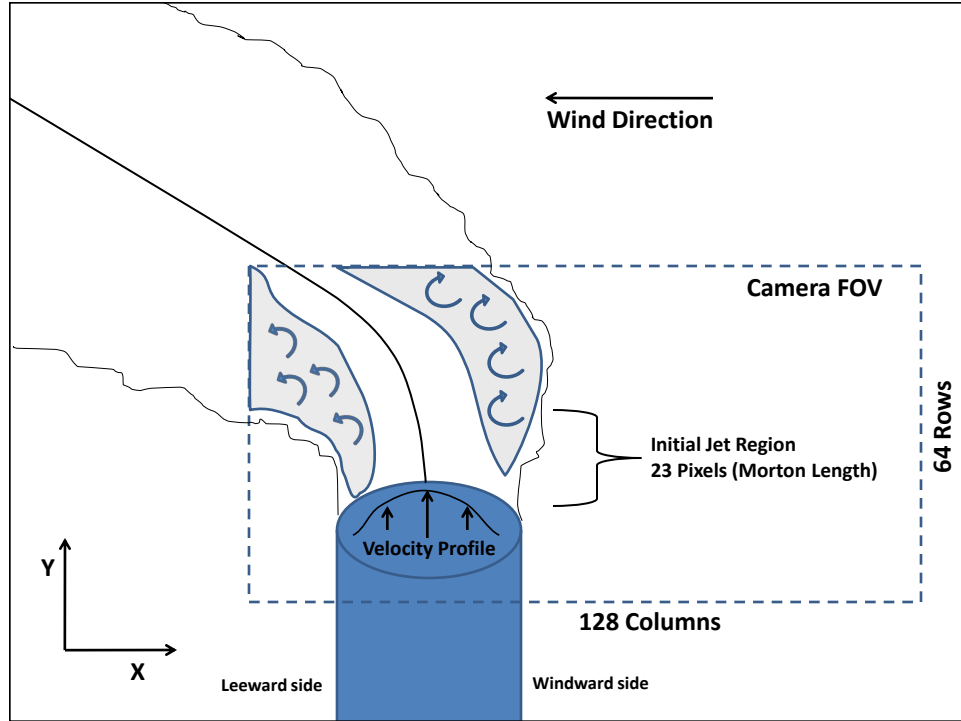
Figure 2. A depiction of the basic behavior of the plume under observation. Video analysis suggests slower moving regions on the windward side of the plume, faster moving regions on the leeward side, and a definite bending almost immediately upon stack exit.

Theory

Plume phenomenology.

Figure 2 is an illustration of the basic flow behavior of the plume being observed. Video analysis of several datacubes shows a definite influence of the wind. The windward side appears to contain regions of stagnation where turbulent puffs tend to hang suspended and are not influenced by the upward flow. The upward flow on the leeward side appears enhanced by the crosswind and bending. In addition, the complication of analyzing a 3D plume with 2D imagery is evident as the leeward side also appears to contain plume particulates which have been swept from the windward side. The behavior seen in the video seems consistent with previous investigation of jets in a crossflow at several jet-to-crossflow velocity ratios. Andreopoulos and Rodi

17

reported on a temperature controlled jet issuing from a circular wall outlet into a cross-stream flowing parallel to the wall. The crossflow in some cases acted like a partial cover over the exit, this caused the jet to bend and initially accelerate on the leeward side while displaying some downwash on the windward side [4]. The nature of the plume studied in this work can be more understood through calculation of the Reynolds number and the Morton length. A flow is typically considered turbulent when the Reynolds number on the order of 1000. The Reynolds number corresponding to this plume is on the order of 10^6, clearly indicating a turbulent flow [7]. When the flow is within one Morton length of stack exit it is considered jet-like and it is considered plume-like at approximately five times the Morton length. Between those two distances the flow is considered transitional [13, 25]. The Morton length for this plume is approximately $2.6\,m$ ($23\,pixels$), so a small initial region of the analyzed flow field is considered jet-like, while the remaining plume within the FPA window is in the transitional region. Based on these fluid parameters, at stack exit this is treated as a turbulent buoyant jet as depicted in Figure 2 [4, 7, 13, 25].

Mass flow rates.

The total effluent mass flow rate can be determined by combining flow field and effluent concentration information:

$$M = \xi \times Q, \tag{1}$$

where M [g/sec] is the desired mass flow rate, ξ [g/m³] is the pollutant concentration, and Q [m³/sec] is the volumetric flow rate [28]. The pollutant concentration is estimated using the simple radiative transfer model as developed by Gross *et al.*, and the flow rate is determined by combining flow velocity and smokestack cross-sectional area:

$$Q = V \times A, \tag{2}$$

where V [m/sec] is the velocity at the stack exit, and A [m^2] is the area. The plume cross-section is assumed equal to the area of the smokestack at the exit, which is known *a priori* in this case but also easily estimated from the IR imagery. The velocity is calculated separately through flow field fluctuation analysis. It is the calculation of both the effluent concentrations and plume flow velocity which require unique models and methods for determination; the remaining parameters of the total effluent mass flow rate are all simple calculations from available data.

Concentration estimation.

As explained above, the simple radiative transfer model for estimating effluent concentrations using the Telops Hyper-Cam developed by Gross *et al.* is used in this work. This model represents the radiance of a given pixel as

$$L\left(\tilde{\nu}\right) = \int \tau\left(\tilde{\nu}'\right) \varepsilon\left(\tilde{\nu}'\right) B\left(\tilde{\nu}', T\right) ILS\left(\tilde{\nu} - \tilde{\nu}'\right) d\tilde{\nu}', \tag{3}$$

where τ denotes the atmospheric transmittance profile along the LOS to the plume, ε represents the spectral emissivity of the plume, B is Planck's distribution for black-body radiation at temperature T, and ILS is the instruments line shape function. This simple model assumes the plume is in local thermodynamic equilibrium (LTE) and ignores scattering, background radiation, and atmospheric self-emission. The spectral emissivity is expressed as

$$\varepsilon\left(\tilde{\nu}\right) = 1 - exp\left(-\sum_i q_i N \sigma_i\left(\tilde{\nu}, T\right)\right) \tau_p. \tag{4}$$

Here, q_i represents the product of the volume fraction ξ_i and the pathlength

19

through the plume l and the quantity $q_i = \xi_i l$ is known as the "fractional column density" [9]. N is the total gas density $[molec \cdot cm^{-3}]$ and related to the plume pressure P (assumed equal to the atmospheric pressure) and temperature T via the ideal gas law. σ_i is the absorption cross-sections of a species as computed by the line-by-line radiative transfer model (LBLRTM) using spectral line parameters from the 2004 (HITRAN) database. The cross-sections were computed every $1\,K$ between $300 - 425\,K$ on the highly sampled ($\delta\tilde{\nu} = 0.0005\,cm^{-1}$) spectral interval: $1750 \le \tilde{\nu} \le 3150\,cm^{-1}$. Factored into the absorption cross-section is the Boltzman distribution which determines the relative population associated with each internal energy level. The total transmittance due to all gas phase plume constituents is represented by the exponential term, and the final term τ_p is the transmittance of the particulate. Since the plume geometry can be inferred from the imagery, the pathlength l will be factored out of q_i so that species concentrations ξ_i can be determined and used in Equation 1 to calculate the total mass flow rate [9].

Velocity estimation.

The temporal information provided by the camera framerate and the spatial data provided by the known pixel FOV supply the information required to estimate plume velocity [32, 21, 10]. They can be combined to calculate a flow velocity as,

$$V = (P \times D) \times \left(\frac{Fr}{OPD} \right), \tag{5}$$

where $P\,[number]$ is the number of pixels traveled by a particular feature, $D\,[\mathrm{m}/\mathrm{pixel}]$ is the known distance per pixel. Framerate and OPD are equivalent in the case of the Hyper-Cam. A single datacube is created through a complete scan (forward and back to initial point) of the Michelson mirror, and at each OPD an image of the plume is recorded. The total number of OPD in the scan is essentially the number of
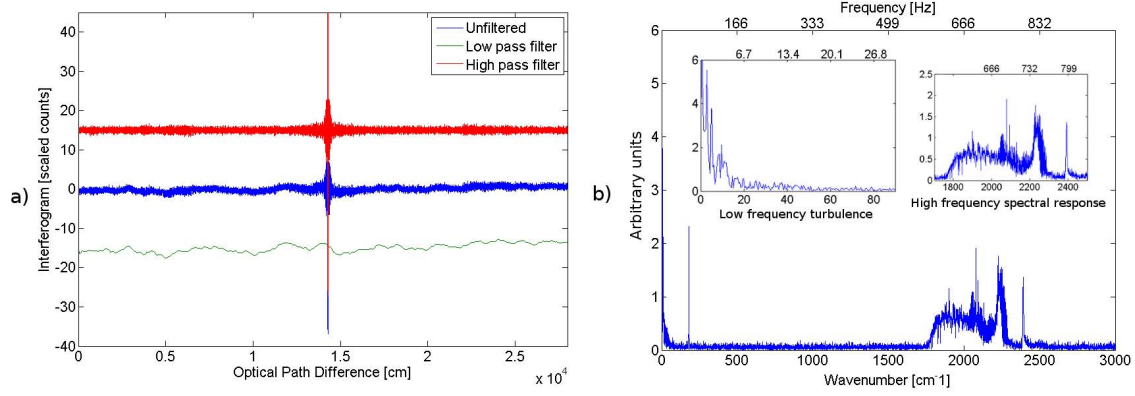
Figure 3. *a)* **Plot comparison of a** $560\,cm^{-1}$ **high-pass filter (top),** $80\,cm^{-1}$ **low-pass filter (bottom) and an unfiltered interferogram (middle) from a pixel in the central flow region.** *b)* **Plot of the corresponding spectrum. The expanded region on the upper left contains the lower frequency plume fluctuations which are evident on the lower interferogram in Plot a). The expanded region on the upper right is the spectral response of the detector which corresponds to the upper interferogram in Plot a).**

frames recorded for that cube. The average framerate is then equal to the length of time required for a complete scan divided by the total number of frames (or OPD) recorded. In Equation 5, Fr [$^{OPD}/_{sec}$] is the average framerate of the camera, and OPD [$number$] is the number of frames a feature shifts along the OPD axis of the datacube as it travel between pixels.

Changes in the flow field yield fluctuations in scene radiance, these fluctuation features can in principle be tracked between neighboring pixels. However, the action of the Michelson interferometer systematically modulates the intensity on the FPA as a function of OPD. Fortunately, the intensity fluctuations due to the Michelson occur at a much higher frequency than that of the turbulence in the plume due to the speed at which the mirror moves. As a result, a temporal low-pass filter (LPF) can be applied to the data to recover the broadband IR imagery. As seen in Figure 3a, the higher frequency responses of the detector to the effluent spectrum has been removed by applying a LPF to the interferogram. The InSb FPA has a spectral response which starts near $1750\,cm^{-1}$, as shown in Figure 3b. By applying the LPF at $80\,cm^{-1}$ the noise of the higher spectral response is removed, and the slower fluctuations due to
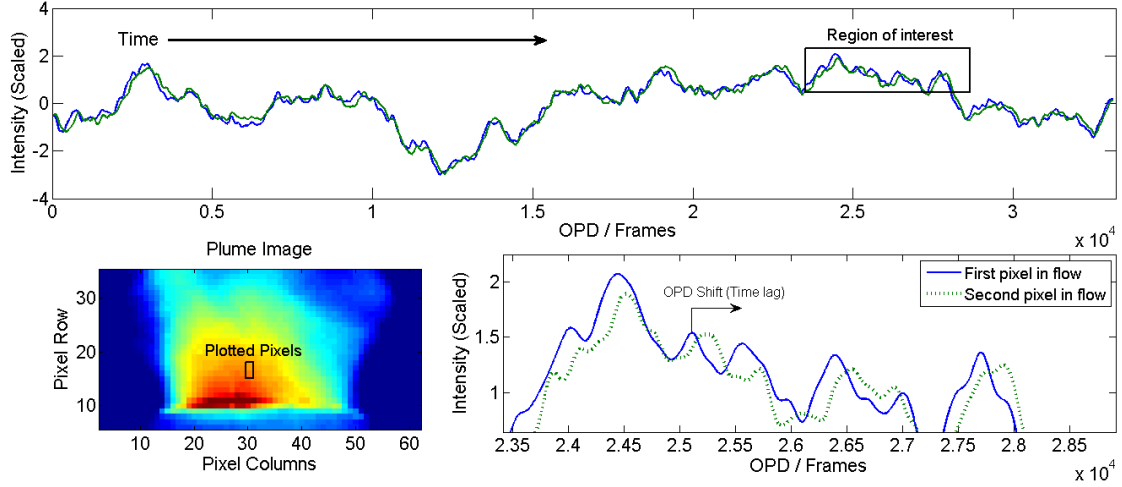
Figure 4. *Top:* Scaled intensity plot versus OPD of two adjacent pixels in the plume flow field. *Bottom Left:* Image of plume and location of plotted pixels. *Bottom Right:* Expanded view of the boxed region of interest from complete intensity plot above. Most features from pixel 1 are duplicated in pixel 2 but shifted along the OPD axis.

the plume flow field can be visualized. The spike at approximately $180\,cm^{-1}$ $(60\,Hz)$ on the spectral plot is an artifact of the camera's cryo-cooler; the LPF has been set at $80\,cm^{-1}$ $(27\,Hz)$ in order to avoid this feature while retaining as much plume fluctuation behavior as possible. Filtered interferogram plots of the type seen at the bottom of Figure 3a are used for comparison between neighboring pixels. The rise and fall of the scene radiance represented along the OPD (temporal) axis form the patterns which can be tracked and correlated. Figure 4 demonstrates the idea behind this method with a comparison between two subsequent filtered pixels in the plume's central flow region.

The upper plot of Figure 4 illustrates the similarities between the two pixels over all OPD as the plume flows over time. It is the applied LPF which allows the brightness fluctuations due to the plume to be seen. To more readily compute the correlation between neighboring pixels, the data is first scaled by subtracting the mean of each vector and dividing by the standard deviation. Without this adjustment, the small OPD shift as compared to the unscaled intensity data goes otherwise undetected

[10, 21, 32]. When a region of interest is expanded and examined more closely, a shift along the OPD axis is evident. The second pixel, further along the flow, repeats the brightness patterns found in the first pixel, but with a delay along the OPD (temporal) axis as the flow moves spatially from one pixel to the next. This shift is equivalent to finding an object at a different location in a film several frames later. A temporal cross-correlation between two vectors along their entire OPD axes can reveal the shift which most closely aligns the two while maximizing the correlation coefficient. Prior to deployment for smokestack data acquisition, the Telops was used to examine a thermal plume generated by a heated laboratory blower. This afforded a velocity estimate of $783 \pm 5\,\mathrm{cm/s}$ which compared favorably with the $800.0 \pm 24.0\,\mathrm{cm/s}$ measured by an anemometer. While this was a controlled environment and certainly not a duplication of field conditions, the excellent agreement between estimated and known values demonstrated the validity of the method to estimate flow rates. In addition, the brightness feature method was fairly straightforward and not computationally intensive, making it a good compliment to the radiative transfer model developed in the effluent concentration work. The laboratory data plots were visually examined for OPD shifts between the more prominent features throughout neighboring pixels. This was suitable for a simple verification of the method with a smaller dataset, but a computational method was required and developed for the large-scale dataset gathered from the smokestack study as described below.

Figure 5 is a typical plot of the correlation between two neighboring pixels treated as a function of the normalized cross-correlation between any two random, jointly stationary, discrete processes defined by:

$$
C_{p_1,p_2}(l) = \begin{cases} \sum\limits_{z=1}^{N-l-1} \frac{p_1(z+l) \cdot p_2(z)}{|p_1||p_2|} & l \geq 0 \\ C_{p_1,p_2}(-l) & l < 0 \end{cases},
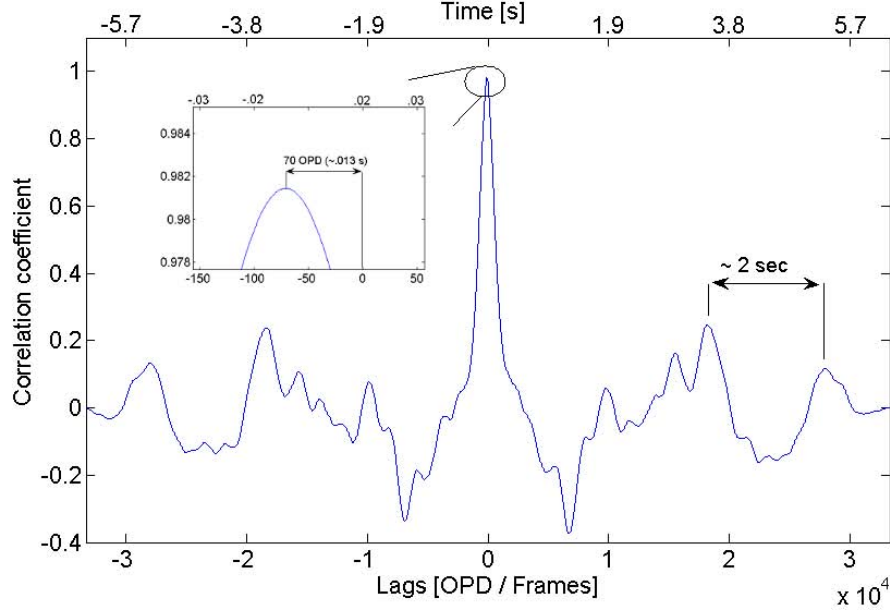\tag{6}
$$

Figure 5. The results of a correlation between two neighboring pixels along center column in the plume flow. The pixels were highly correlated at a lag of approximately $70\,OPD$. Underlying correlation sub-maxima are evident in the plot and may be indicative of additional flow field information.

where p_1 and p_2 are the spatially separated pixels on the FPA, z is the OPD or temporal axis at each pixel, l is the lag value, and N corresponds to the total number of frames, or OPD, along the z axis. The function sequentially sums the dot product between the two pixels while taking lag steps along the temporal axis and returns a $C(l)$ vector of size $2N-1$. It is normalized to return a value of one at zero lag when correlating identical vectors [26, 24]. The Y axis in Figure 5 corresponds to the degree of correlation at the separate lag values displayed on the X axis. The location on the X axis corresponding to the maximum correlation value indicates the OPD lag between the two vectors, and it is this value which is converted to the temporal component used in velocity calculation. This process is used specifically to determine only the shift which gives arise to the maximum correlation, but the additional smaller maxima on the plot may reveal additional information about the flow behavior. For instance, the Strouhal number is a dimensionless value which may

24

be determined through analysis of the underlying frequencies found in Figure 5 and can prove useful in classifying turbulent length scales. It is defined as $St = \frac{f \times D}{V}$, where D is the exit diameter, V is the fluid velocity, and f is a frequency associated with the oscillatory fluid behavior. Estimating the distance between sub-maxima in Figure 5 at approximately $10,000\,OPD$ or $2\,sec$ translates to a frequency of $\sim 0.5\,Hz$. This frequency, with the *in situ* values of V and D, produces a Strouhal number of approximately 0.29. This is on the order of a value expected for a plume with such a high Reynolds number and reasonable enough to assume additional flow field information may be extracted using this type of temporal data [20, 29]. The focus of this work is to determine volumetric flow, but the possibilities of turbulent flow field analysis through the estimation of some of the more defining length and time scales using IFTS is an attractive option for future studies.

When combined with the camera's framerate, this frame (or OPD) shift leads to the temporal aspect of velocity. The pixel number P, from Equation 5, is determined by examining the difference between pixels selected for correlation; a pixel compared with the subsequent pixel in the row above would result in a P value of 1. The pixel number, combined with the known translated pixel size, gives the spatial relationship. This, along with the temporal information gained from the OPD shift, leads to an estimate of the plume flow velocity.

Due to the complications introduced by the flow and turbulence of a thermal plume, the region in which to estimate flow velocity is not easily determined. It is known the radial velocity profile of a plume generally drops off when drifting from center axis [5, 23, 4]. The analyzed images in this work are a 2D representation of what is in reality a 3D flow, therefore the intensity being analyzed at any one pixel represents an integration along a LOS through the plume and the velocity profile in that third dimension. The impact of this effect on the velocity estimation is

unknown, but it is hoped a mean flow velocity can be found by averaging over a large number of individual datacubes. In addition, wind effects of the type depicted in Figure 2 appear to have a strong influence on flow behavior. The exact effect of the crosswind on the upward flow velocity is not known, but it is assumed that the region near center is most shielded. In order to best estimate the plume's inner stack velocity without incorporating a computationally intensive turbulence model which could possible account for crosswind and velocity gradients, the center of the plume alone was analyzed. The specific pixels from the center column to use in estimation were established during analysis and are described and justified in the velocity results section below. While this approach is not being asserted as ideal, it is expected to be a reasonable enough tactic to demonstrate the potential of IFTS in the flow field analysis regime.

Results

Concentrations.

The 185 interferogram cubes were first time-averaged to improve the (SNR). Figure 6 is a time-averaged spectrum from a pixel at row 17, column 32 above the stack exit. This pixel has been selected due to its location in the initial region used for flow field analysis as described in the velocity results below. As with the 2008 data, strong emissions from H_2O, CO_2, CO, SO_2, and NO are evident. The top panel is the complete spectrum at that pixel after background subtraction. The background spectrum was taken from an average of columns 80:120 in row 17, well outside any influence from the plume. The bottom panel is a plot of the transmittance profile over the $300\,m$ path from plume to camera. As expected, the absorption features are largely due to H_2O and CO_2 [9]. With effluent identification in agreement with the initial Telops study, the model was fit to the new dataset. For each pixel in row 15
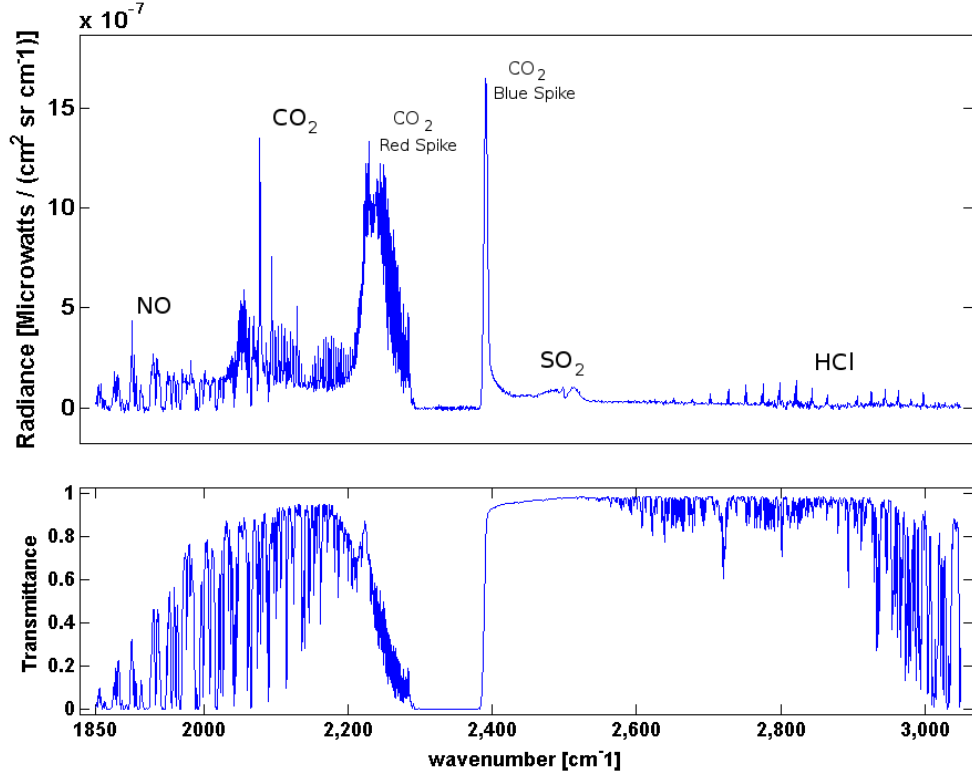
Figure 6. *Top Panel:* **Time-averaged spectrum from pixel** $(R, C = 17, 32)$**. The regions in which** H_2O**,** CO_2**,** CO**,** SO_2**, or** NO **were identified are annotated.** *Bottom Panel:* **The atmospheric transmittance profile for the** $300\,m$ **LOS from instrument to tip of stack.**

above the stack, column densities, particulate transmittance and temperature were estimated by fitting Equation 3 using a Levenberg-Marquardt nonlinear minimizer. While the final results with this dataset are in reasonable agreement with *in situ* measurements, uncertainty values are much higher than expected.

Figure 7 contains the fit results from pixel $(R, C = 15, 32)$ above the stack. As can be seen in the figure there still appears to be structure in several areas of the residuals, but it is an improvement over initial fit attempts. It is difficult to determine the exact cause of the additional systematic error, but the setup and environmental conditions may have had more effect on the results than originally expected. As described in the experimental section, the Telops Hyper-Cam was stationed $350\,m$ from stack exit, the background was uniformly cloudy throughout data capture with a $3.6\,\mathrm{m/s}$ wind

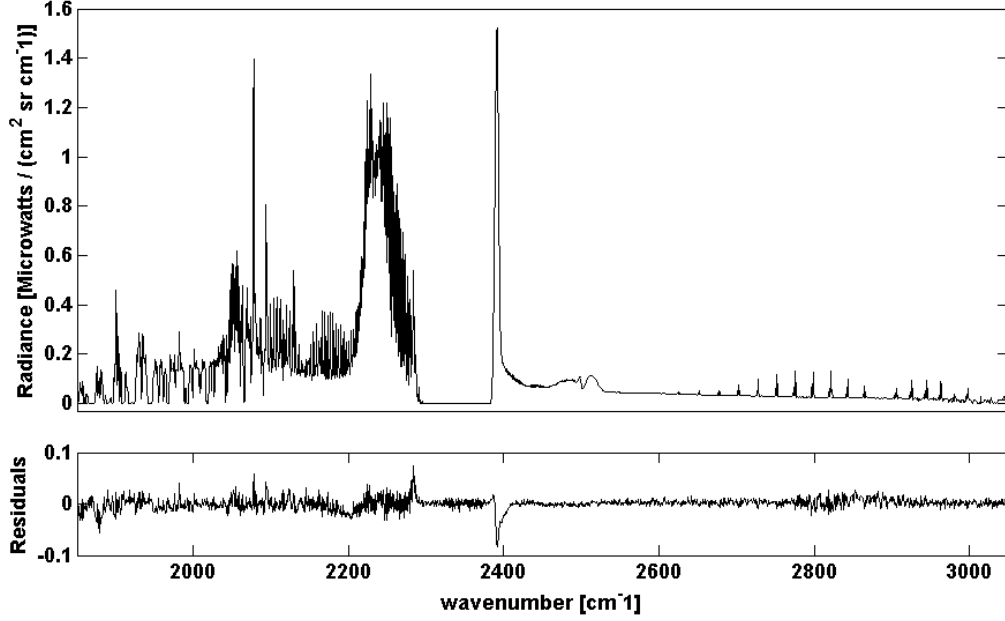**Figure 7. Spectral fit and residuals for central pixel (R,C = 15,32). A more complete model was applied to the dataset to improve concentration accuracy and fit residuals. While concentration values improved, a great deal of structure can still be seen in the residuals.**

(at $10\,m$) nearly perpendicular to the LOS, and the camera's spectral resolution was set to $0.5\,cm^{-1}$. Conversely, in the 2008 data capture the camera was $595\,m$ from the stack with a uniformly clear sky and only a $0.9\,\mathrm{m/s}$ wind, and the spectral resolution was set to $0.25\,cm^{-1}$. The lower spectral resolution may have had some effect on the residuals, but column density results seem to indicate the wind conditions may have been very disruptive and influential on systematic error.

The top of Figure 8 is a plot of the peak normalized SO_2 column density across Row 15 above stack exit. Imagery analysis has given an approximate stack exit spanning columns 14 to 50, and this plot represents the pixels in that range. The column density was expected to be representative of the stack geometry, as was found with the 2008 dataset. As described in the theory section above, column density is related to pathlength as $q_i = \xi_i l$, where ξ_i represents particulate concentration and l is pathlength through the plume. Column density should then appear to uniformly
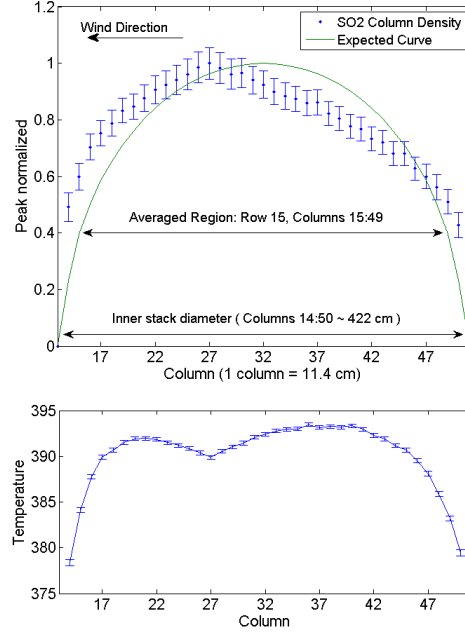
Figure 8. *Top:* **Peak normalized** SO_2 **column density** (q_i) **fit values across stack exit (Row 15, Columns 14:50). The solid, smooth curve represents the expected plot as column density drops under the influence of a reduction in plume pathlength.** *Bottom:* **Fitted temperature values across the same stack region.**

drop with movement off the central axis, and the peak value would ideally reside at the center column, as represented by the smooth expected curve included in the figure. The smooth curve represents the variation in column density expected if the plume shared the cylindrical geometry of the stack; it is normalized by the imagery estimated plume pathlength (approximately $422\,cm$) at column 32. The fitted results indicate an obvious shift to the left of the plume center, with the peak instead near column 27. Left of that point there appears to be curvature which is more suggestive of stack geometry, but right of the peak the values drop significantly. This seems to indicate column density is being influenced by the wind at the stack. These wind effects coincide with those seen in the analysis of stack flow velocity below and likely contributed to the systematic error in the fit results. Due to their stack edge locations on either side of the plume, columns 14 and 50 had a negative effect on results, therefore only columns 15 to 49 were used to determine volume mixing fractions. The

Table 1. Comparison of estimated volume mixing fractions($\xi_i = q_i/l$) with *in situ* measurements. Only CO_2, SO_2, and $NO_x (NO + NO_2)$ were monitored and reported. *In situ* plume transmittance is not listed in this table. It was provided indirectly via the opacity data measured in the visible, and may not correspond to the MWIR estimated transmittance.

Parameter (units)	units	ξ_i value	ξ_i error	*in situ* value	*in situ* error
CO_2	%	9.32	1.5	8.49	0.04
H_2O	%	7.16	1.27	−	−
SO_2	ppm	349.97	55.0	352.356	2.27
NO	ppm	162.96	20.7	−	−
$NO_x = NO + NO_2$	ppm	−	−	120.19	1.67
HCl	ppm	62.57	10.2	−	−
CO	ppm	34.96	5.23	−	−
τ_P	-	.98	0.005	-	−

bottom of Figure 8 is the fitted temperature plot in the same region. Temperature appeared uniform across the stack in the 2008 data, but here it varies throughout and is obviously lower toward the edges. The mean temperature is $391\,K$ with a standard deviation of $2.5\,K$. The remaining particulates were fitted across row 15 and results were similar in each case; however, it was still possible to extract reasonable concentration values.

With a column density at each column along row 15 and a knowledge of plume pathlength at each point, it was possible to extract concentrations, $\xi_i = q_i/l$. The value for l at each pixel can be taken from the smooth curve in Figure 8, which is normalized to the pathlength through center plume. Table 1 contains a summary of final fit results. Estimated values are within reasonable agreement, but error is consistently higher than desired. The spectral error is the standard deviation found when averaging each effluent across plume pixels in Row 15 and may be large due to wind effects of the type seen in Figure 8. The standard deviation is at or above 15% of the final spectral estimate in most cases. CO_2 and SO_2 values are in reasonable agreement with reported values, but the large estimate of NO in relation to the

smaller reported NO_2 is not understood. NO values in the 2008 experiment were below the total reported NO_x values, as would be expected. *In situ* error is actually the standard deviation stemming from the averaging of the values reported throughout the observation period. The combination of temperature fluctuations, odd geometric variation in q_i with plume location, and structured residuals seem to indicate some true systematic errors with the spectral analysis. These may be caused by a combination of wind and sharp look angle relative to wind direction. Considering the model dependence on the assumed homogeneity of the plume in any particular pixel location, a strong wind which may be causing additional mixing of effluents could result in systematic error of the type found here. An improved model of the plume geometry in a crosswind which includes thermal and concentration gradients along the LOS could potentially reduce these systematic errors [25, 23].

Velocity.

Equation 5 in the theory section above characterizes the method to determine the velocity in the flow field. The number of pixels over which a feature was tracked (P) and the computed distance per pixel (D) provide the spatial data to estimate plume velocity, while the temporal data is provided by the camera's frame rate (Fr) and number of OPD (frames) the feature shifted between pixels (O). While O and P were determined through analysis of the flow field, D and Fr could be calculated from available data. As described in the experimental section, each pixel has a FOV of $0.326\,mrad$. At $350\,m$, the 64×128 pixel subset translates to a $0.114 \times 0.114\,m^2$ area per pixel at the top of the stack. Therefore, the single pixel distance traveled by a brightness feature in only the Y direction was taken as $D = 0.114\,m$. The average camera frame rate of $5.26\,kHz$ was used in the velocity calculation as a value for Fr.

As mentioned in the theory section above, the center region of the plume flow
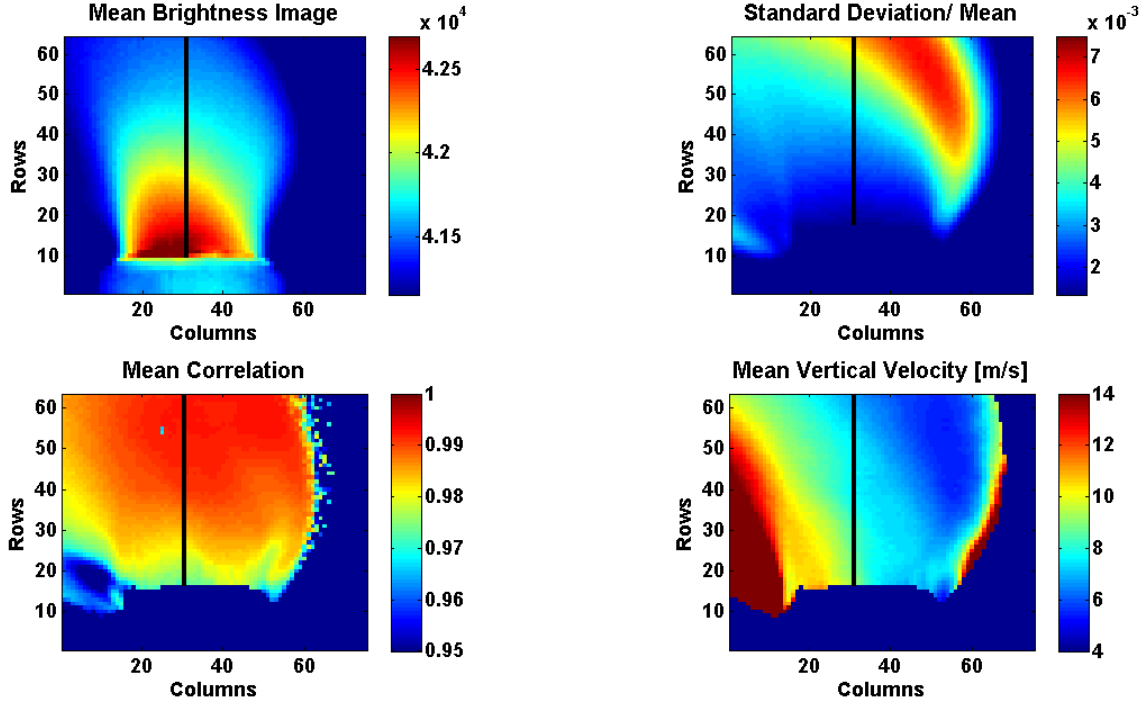
Figure 9. *(Top Left):* Mean brightness image averaged over all 185 datacubes in arbitrary units. The black line denotes the center of the stack (Column 32). *(Top Right):* The mean coefficient of variation (standard deviation divided by the mean) over all cubes. This image led to an additional windowing of the flow velocity estimation region to rows 17 through 63 as indicated by the adjusted black line. Regions below $0.0014\,(3 \times Background)$ were used to mask the images in the bottom row. *(Bottom Left):* Map of the mean correlation coefficients resulting from the feature tracking method. All pixels used to determine OPD shift for velocity estimation were highly correlated. *(Bottom Right)* Final map of average estimated plume flow velocity in the Y (upward) direction.

would be analyzed for velocity estimation. For reasons explained below, each pixel would be correlated to the one directly above, which sets P equal to one. As seen in Figure 9, column 32 (denoted by the bold black line in all four subfigures) is a reasonable estimation of stack center. All images are the result of averaging the total set of imagery over all frames from each of the 185 data cubes; approximately 6 million images were used to generate any single, mean image. The image at top left is the mean IR image of the stack and plume. The effects of the wind from right to left are evident but not pronounced, and the stack can easily be discerned

in this image, making center estimation fairly simple. The image at top right is the average coefficient of variation (standard deviation divided by the mean). This image reveals a lack of variation with regard to the mean in the region above stack exit. However, the proposed brightness feature tracking method is dependent on fluctuations in the plume, and it was unclear whether this region would provide an accurate picture of flow behavior when analyzed using such a method. Therefore, average background values were calculated from column 110 (not shown, but well outside the influence of the plume), and in order to emphasize the regions of greatest deviation, the pixels below 0.0014 (three times the background value) were used to create a mask for the images in the bottom row of Figure 9. This resulted in beginning the velocity estimation at row 17, as is indicated by the adjusted black line in this and the remaining images. The image at left on the bottom row is a map of the average correlation coefficients which were calculated using the feature tracking method described in Figures 4 and 5 found in the theory section above. It should be noted initial analysis included correlation with multiple pixels in the rows above a given pixel at center stack, and the greatest correlation was typically not directly above. A leftward shift was generally evident, angling the line of greatest correlation to the leeward side. Future work should address improving the slight off-vertical flow direction estimation when strong crosswinds are present. The current model is best suited for correlation directly above, and it was decided this would be suitably indicative of the upward velocity while still demonstrating the validity of the method. The OPD (temporal) axis of each pixel in the 64×128 array was therefore correlated to the one directly above. Despite the actual leftward diagonalization of the maximum correlation just described, the pixels correlated to those directly above as seen here are highly correlated throughout the plume itself (coefficients of 0.95 or greater) and are especially high in the region chosen for analysis. The corresponding

33

OPD shifts calculated from these correlations were used to calculate velocities using Equation 5. The final image in Figure 9 maps those calculated velocities throughout the plume flow field. These velocities are a result of correlating each pixel to the one directly above, therefore it is only indicative of the flow in the Y (upward) direction. The specific velocities from the analysis region are plotted in Figure 10.
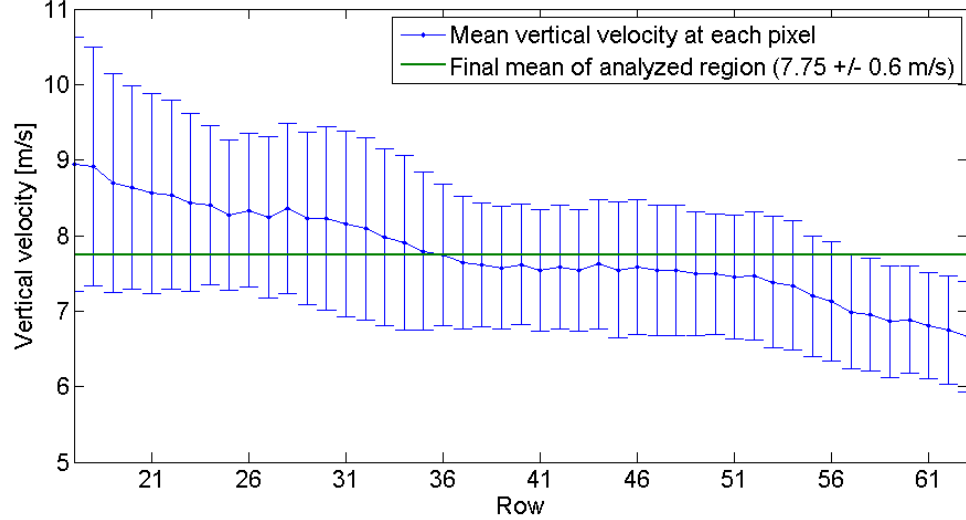

Figure 10. Plot of the average vertical velocities per pixel from the final region used for flow field velocity analysis: column 32, rows 17:63. The error bars are derived from the standard deviation over the 185 datacubes averaged at each pixel in the column. The mean velocity in this region (green line) was found to be $7.75 \pm 0.6\,\mathrm{m/s}$, where the error is derived from the standard deviation along that column.

There is a slow decrease in velocity with an increase in distance from the stack along the plume's central axis in Figure 10. These results are in reasonable agreement with the velocity profiles found in studies of jets and plumes. Andreopoulos and Rodi reported on a temperature controlled jet issuing from a circular wall outlet into a cross-stream flowing parallel to the wall. Remaining on central axis above exit, vertical velocity tended to drop as distance from the source increased [4]. In his review of turbulent jets and plumes, List also found axis velocities of round heated plumes (not in a crossflow) to begin an on-axis drop in magnitude with distance from flow exit [23, 12]. This lends some validity to the temporal cross-correlation

method chosen here, although additional analysis of plumes in a controlled laboratory environment would assist in maturing the model. The ability to locally measure rates throughout the flow in an applied, controlled crossflow would perhaps allow a better understanding of the diagonalized maximum correlation and it could be reliably incorporated as an exact mapping of the velocity in both the X and Y dimensions.

The final mean value of Figure 10 was found to be $7.75 \pm 0.6 \, \mathrm{m/s}$, where the uncertainty is determined by the standard deviation from the mean along that column. This velocity is used to calculate the plume's volumetric flow rate, which is combined with the spectral concentrations for total effluent mass flow rates. Each datacube produced a velocity at each pixel, the error bars in Figure 10 represent the standard deviation of the averaged velocities over the 185 datacubes. As described above, the wind had an influence on the vertical velocity and caused fluctuations which likely contributed to systematic error. It is possible some of the systematic error could be removed by fully developing a more robust model as described above. This would allow for analysis of the velocity in the natural direction of the flow and vertical stack velocity could be determined through vector subtraction of the wind component. Finally, the turbulent behavior of a thermal plume in this region no doubt has a number of effects on the flow and velocity in any one direction as well [5, 8, 19, 33]. The primary purpose of this study is to determine the validity of the proposed brightness feature tracking method. Further analysis of the rows plotted in Figure 10 for fluid dynamic effects was therefore deemed beyond the scope of this work. However, the imagery suggests further analysis is certainly possible and lends weight to the potential of interrogating thermal turbulent plumes using IFTS in future work. MCC techniques in particular may be ideal for analysis of turbulence and movement throughout the entire plume [3, 17, 16, 27, 30].

Table 2. Comparison between estimated and reported total effluent mass flow rates in kilograms or grams per second.

Parameter	units	2010 M value	2010 M error	2010 in $situ$ value	2010 in $situ$ error
CO_2	kg/s	13.5	3.78	11.6	0.07
H_2O	kg/s	7.76	2.25	–	–
SO_2	g/s	71.3	19.3	67.8	0.52
NO	g/s	16.1	4.19	–	–
NO_x	g/s	–	–	11.2	0.16
HCl	g/s	7.40	2.0	–	–
CO	g/s	15.0	4.05	–	–

Total mass flow rates.

As detailed in the theory section above, the volumetric flow rate in Equation 18 is determined by combining flow velocity and smokestack cross-sectional area. Examination of the flow field near the stack exit in Figure 9 reveals an inner diameter which approximately spans columns 14 to 50, leading to an estimated 37 ± 0.5 pixels. Using the translational pixel size of $.114\,m^2$, this leads to an exit diameter of $37 \pm 0.5\,pix \times .114\,\mathrm{m}/\mathrm{pix} = 4.22 \pm 0.6\,m$, and a cross-sectional area of $14.0 \pm 2.8\,m^2$, which is in excellent agreement with the in $situ$ value of $14.1\,m^2$. The final estimated volumetric flow rate based on these values is $Q = 7.75 \pm 0.6\,\mathrm{m}/\mathrm{s} \times 14.0 \pm 2.8\,m^2 = 106 \pm 23\,\mathrm{m^3}/\mathrm{s}$. This is in excellent agreement with the in $situ$ value of $Q = 102 \pm 0.4\,\mathrm{m^3}/\mathrm{s}$, where the uncertainty is the standard deviation of the reported values recorded during data capture. The uncertainty in the volumetric flow is almost entirely due to the uncertainty in estimating the number of pixels spanning the inner stack exit. The estimated volumetric flow rate was combined with the concentration values from Table 1 to determine total effluent mass flow rates found in Table 2. The estimation results in Table 2 are in reasonable agreement with the reported values, and the large uncertainty values from both the concentration estimates and volumetric flow rates obviously effected final error. CO_2 and SO_2 estimates are within 16% and

5% respectively, while NO is 44% above the combined NO_x reported value. This is a propagation of the unexplained higher concentrations of NO obtained from the spectrum.

Conclusion

With the advent of IFTS, the already mature capabilities of the passive optical remote sensing field have been greatly enhanced. The ability to access the DC level imagery at each pixel provides a spatial understanding of the target which proves extremely beneficial. Initially, the work done by Gross *et al.* showed the impact this imagery can have on concentration estimation. In that work, using only the Telops Hyper-Cam, fractional column densities were estimated using a single-layer radiative transfer model. The imaging capabilities of the camera made it possible to orient and perform analysis in the ideal region above stack exit, and it was possible to extract effluent volume mixing fractions from the column densities [9]. The success of that effort led to an understanding of the potential unlocked by leveraging the time resolved DC level imagery. The scope of this work was to extend the exploitation of the imagery and merge flow field analysis with the already successful concentration estimation technique to determine a final effluent mass flow rate. A method of tracking brightness features across pixels through a measured number of frames using temporal cross-correlation was employed to determine a velocity. Imagery provided an estimation of stack exit diameter, and the two were merged to provide a volumetric flow rate of $106 \pm 23 \, \mathrm{m^3/s}$ which agreed favorably with the *in situ* value of $102 \pm 0.4 \, \mathrm{m^3/s}$. Although the previously established simple model adopted to estimate concentration values met with some complications and large systematic error, the final mass flow rates were in reasonable agreement with reported values. A manageable method to estimate volumetric plume flow rates to complement the proven simple method

for estimating effluent concentrations has been established. With both pieces of the equation separately demonstrated, it is reasonable to assert the feasibility of IFTS in estimating total effluent mass flow rates from a single data set. Improvements could be made to allow robust analysis of both concentrations and velocity while reducing some of the systematic error found in this work. While it is probably best to keep the standoff distance at or below $350\,m$ to ensure an individual pixel FOV near $10\,cm^2$ for reasonable spatial resolution, camera settings could be geared more for concentration estimation while still allowing flow analysis. The spectral resolution could be increased to the $0.25\,cm^{-1}$ used in the initial concentration estimation effort, and a kHz framerate would still be available. Ideal wind conditions have not been established, but the $6.0\,$m/s wind present during data capture was likely a factor with the error. While wind obviously cannot be controlled, the short time window necessary to capture sufficient data using the Telops should allow future data capture during periods of little to no wind a possibility. Applying the temporal cross-correlation method to only the central column of the plume did allow a reasonable estimation of vertical velocity; however, further development of the model to estimate the flow in two dimensions is likely the best approach.

Just as the initial work estimating concentrations with the IFTS led to the notion of extending the analysis to volumetric and mass flow rates, this work has opened the door to the possibility of examining the turbulent nature of thermal plumes. Spatial maps of the type found in Figure 9 are indicative of the type of turbulence visualization which can be achieved using this tool. Imagery processing methods such as optical flow and particularly MCC could extract a great deal of information about two-dimensional flow and turbulent behavior near stack exit. Future work could look to improve the volumetric flow estimation and possibly incorporate an understanding of buoyancy and plume rise, allowing a single deployment of the Telops

to generate effluent mass flow rates as well as an understanding of their dispersion into the atmosphere. Passive remote sensing has long been a viable method for monitoring of chemical plumes, but the onset of IFTS has established a capability to allow a single device to estimate total effluent mass flow rates. The ability to verify these reported rates from a single remote location in a two hour setup-to-teardown session can prove invaluable to environmental monitoring agencies.

Appendix A. Extended velocity discussion

The purpose of this section is to add additional insight and clarity to the velocity and flow analysis performed in Chapter III. Reasons for windowing the velocity analysis in column 32 were based on the coefficient of variation. As the method for velocity estimation was based on movement of brightness features, it was necessary to examine regions which had legitimate variations in brightness. However, the plot of the estimated velocity to include the masked pixels is interesting and warrants some discussion.

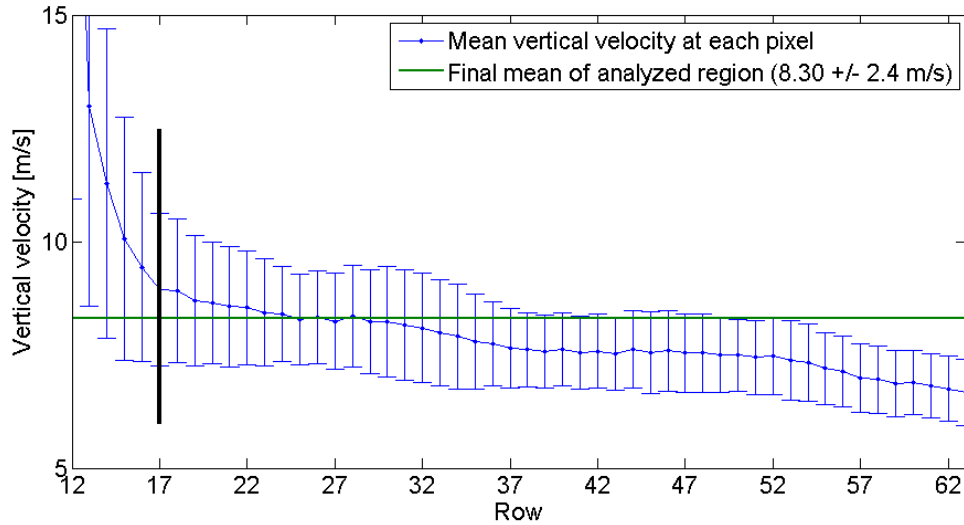Figure 11 is a complete estimated velocity profile of column 32 from stack exit to

Figure 11. Estimated velocity profile of column 32 which includes rows 12:16. These rows were masked by the coefficient of variation during primary velocity analysis but have been included in this plot for consideration.

the final row in the FOV. As mentioned in the results, the decrease in velocity is in agreement with the results of Andreopoulos and Rodi in their investigation of jets in a crossflow, however, the extremely high values near stack exit were not seen in their work and do not seem physically likely [4]. Chen and Rodi's study of thermal round plumes was more indicative of the behavior beyond row 17, but again the extremely
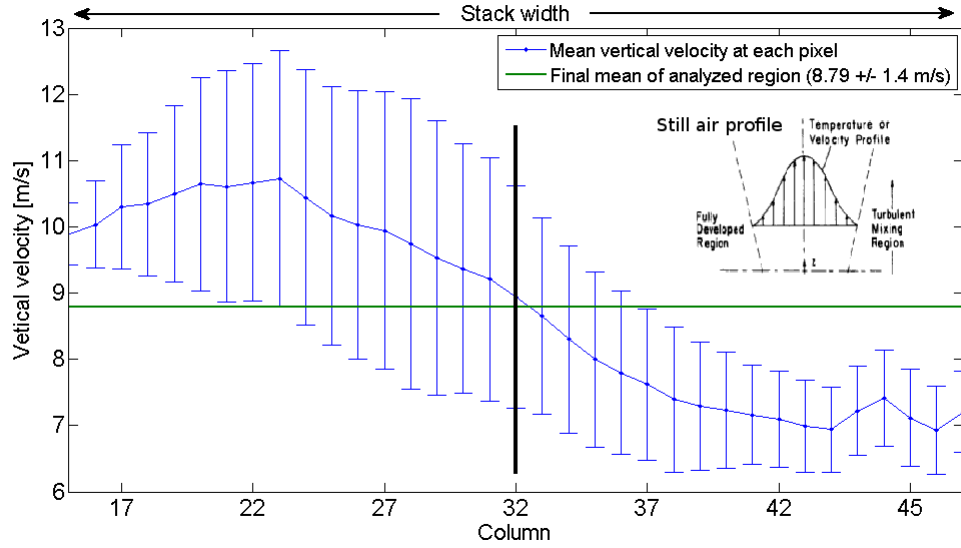
Figure 12. Vertical velocity profile with error bars spanning row 17 above stack exit. Inset is the expected velocity profile from a thermal plume in still air as seen in an examination of thermal and momentum structure by Prengle *et al.* [31].

high exit velocity at stack exit and immediate drop were not seen. Exit velocity was actually sustained initially before beginning a slow decay [12, 23]. These extremely large velocities are more likely indicative of a failure in the brightness feature tracking method to accurately estimate OPD shift in regions of sustained brightness. This further validates the decision to window the first 5 rows from velocity analysis based on variation effects. Sustained brightness as seen near stack exit in the top left image of Figure 9 would wash out the temporal shift required for accurate cross-correlation. This would lead to a minor shift in OPD to maximize correlation; a smaller OPD shift results in a higher velocity, as the two are inversely related.

Figure 12 is a plot of the velocity across row 17, from columns 15 to 49. This is just within the inner stack diameter and at the start of the region chosen for analysis in column 32. In a plume exhausting into still air the velocity profile would be expected to drop in a manner similar to the inset profile displayed in Figure 12. Andreopoulos and Rodi showed the impact a crossflow can have on the windward and leeward side

of a crossflow, and the results in row 17 are similar to those put forth in the study. On the leeward side (left of column 32) velocity is expected to be higher, while the windward side may be influenced by a downwash caused by the crosswind [4]. Due to the differences in experimental setup these results cannot be considered conclusive, but they are indicative of the brightness feature tracking method tracking actual flow velocities in this region. Both the primary and inset velocity profiles in Figure 12 corroborate the decision to maintain velocity analysis at the plume's central axis.

Appendix B. Additional Calculations

The equations and values used in calculating both the Reynolds number and Morton length are given in this appendix.

Reynolds number

The Reynolds number is a fundamental dimensionless number which is related to the turbulence of given flow conditions. It is a relationship between inertial and viscous forces defined as

$$Re = \frac{V \times D}{\nu},\tag{7}$$

where V is the velocity of the fluid, D is the diameter of the stack, and ν is the kinematic viscosity of the fluid [7]. For this calculation the reported flow velocity of $7.23 \, \text{m/s}$ and known stack diameter of $4.23 \, m$ are used. The kinematic viscosity used is that of air at $400°K$ taken to be $25.90 \times 10^{-6} \, \text{m}^2/\text{s}$ [2]. These values give a final Reynolds number of 1.2×10^6.

Morton length

Morton length is a relationship between the momentum and buoyancy fluxes which characterizes the regions of jet-like and plume-like flow:

$$l_m = \frac{M^{\frac{3}{4}}}{B^{\frac{1}{2}}},\tag{8}$$

where M is the momentum flux and B is the buoyancy flux. The momentum flux is defined by $M = A \times V^2$, where A is taken as the diameter of the stack and V is again the reported flow velocity. The buoyancy flux is defined by $B = g\frac{\Delta \rho}{\rho}Q$, where g is gravitational acceleration,$\Delta \rho$ is the difference between fluid and ambient pressure, ρ is the density of the ambient air, and Q is the stack volumetric flow rate of

$102\,\mathrm{m^3/s}$ [13]. For this work, the density relationship was described by the temperature difference between plume and air: $\frac{\Delta\rho}{\rho} = \frac{T_{air}}{\Delta T}$, where T_{air} was taken to be $300°K$ and ΔT to be $100°K$. This resulted in final values of $M = 735\,\mathrm{m^4/s^2}$, $B = 2999\,\mathrm{m^4/s^3}$, and $l_m = 2.6\,m$.

Appendix C. Applicable MATLAB Code

This appendix is intended to present and explain code specific to the brightness feature tracking method. Each set is individually summarized, and any necessary comments in the code are made where necessary for clarification using standard MATLAB (%) comments.

Correlation of pixels

Each pixel in the 64×128 array is correlated with the one above. This correlation is accomplished over the third dimension of the datacube which corresponds to the temporal (OPD) axis. The function pixel_comparisonup.m was created to handle the correlation; it requires a datacube which has already received a low pass filter. The function returns 2 separate 63×128 matrices: one a map of the OPD shift which supplies the maximum correlation (pixcorr) and the other a map of the corresponding correlation coefficients (pixcoeff).

```
function [pixcorr,pixcoeff] = pixel_comparisonup(Data)
% The initial 150 OPD are cropped from the data; the imagery in that region
consistently contained artifacts and were not indicative of true data
Plume = Data(:,:,150:end);
[row column frame] = size(Plume);
% The data is then scaled along the OPD axis using the zscore function. As de-
scribed in the results section, this scaling is necessary to accomplish cross-correlation
z = zeros(row, column, frame);
for ii=1:row for jj=1:column
    tmp = zscore(squeeze(Plume(ii,jj,:)),[],1);
    z(ii,jj,:) = tmp;
% "z" is the scaled matrix to be passed into the cross-correlation loop
```

end

end

% Create cross-correlation matrices

% "maxcorr" prevents MATLAB from attempting to find an OPD shift greater than 2000

maxcorr = 2000;

[row column frame] = size(z);

pixcorr = zeros(row-1,column);

pixcoeff = zeros(row-1,column);

for ii = 1:row-1

for jj = 1:column

tmp = xcorr(z(ii,jj,:),z(ii+1,jj,:),maxcorr,'coeff');

% Final correlation value is corrected to report exact OPD shift

[pixcoeff(ii,jj) pixcorr(ii,jj)] = max(tmp); pixcorr(ii,jj) = 2000 - pixcorr(ii,jj) + 1;

end

end

end

% end of pixel_comparisonup.m

The pixel_comparisonup.m function is used to generate a pixcorr and pixcoeff matrix for each of the 185 datacubes. These are combined to create two final matrices which are $63 \times 128 \times 185$ and averaged to get a mean velocity.

% Get the average OPD shift at each pixel over all 185 cubes

corrave(:, :) = nanmean(pixcorr, 3);

% Get the accompanying average correlation coefficients

coeffave(:, :) = nanmean(pixcoeff, 3);

% Define the previously computed average frame rate

Fr = 5260;

% Convert the OPD shift matrix to a velocity matrix using pixel size and frame rate as defined in Equation 5; this creates an average velocity value at each pixel in $^{m}/_{s}$

velave = (.114*Fr) ./ corrave;

The average velocity values in Column 32, Rows 17:63 of matrix velave were used to generate Figure 10 and to establish the mean velocity used for volumetric flow rate calculation.

Bibliography

[1] "Location Weather History", August 2010. URL http://www.wunderground.com.

[2] "Air - Absolute and Kinematic Viscosity", January 2011. URL www.engineeringtoolbox.com.

[3] Aksu, Ibrahim, Fatih Ildiz, and Jeff B. Burl. "A Comparison of the Performance of Image Motion Analysis Algorithms Operating on Low Signal to Noise Ratio Images". *IEEE*, NA:NA, 1992.

[4] Andreopoulos, J. and W. Rodi. *Journal of Fluid Mechanics*, volume 138. Cambridge University Press, 1984.

[5] Antonia, R.A., A. Prabhu, and S.E. Stephenson. *Journal of Fluid Mechanics*, volume 72, part 3. Cambridge University Press, 1975.

[6] Beychok, Milton R. *Fundamentals of Stack Dispersion*. Beychok, 2005.

[7] Blackadar, Alfred K. *Turbulence and Diffusion in the Atmosphere*. Springer-Verlag Berlin Heidelberg, 1997.

[8] Boguslawski, L. and Cz. O. Popiel. *Journal of Fluid Mechanics*, volume Vol. 90, part 3. Cambridge University Press, 1979.

[9] Bradley, Kenneth C., Kevin C. Gross, and Glen P. Perram. "Remote identification and quantification of industrial smokestack effluents via imaging Fourier-transform spectroscopy". *Environmental Science and Technology*, NA:NA, 2010.

[10] Buchhave, Preben. "Particle Image Velocimetry-Status and Trends". *Experimental Thermal and Fluid Science*, 5:586–604, 1992.

[11] Chamberland, M., V. Farley, A. Vallieres, A. Villemaire, L. Belhumeur, J. Giroux, and J.-F. Legault. "High-performance field-portable imaging radiometric spectrometer technology for hyperspectral imaging applications". *Proceedings of SPIE*, 59940N. 2005.

[12] Chen, C. J. and W. Rodi. "Vertical turbulent buoyant jets: A review of experimental data". *HMT Science and Applications of Heat and Mass Transfer*, 80:94, 1980.

[13] Crone, Timothy J., Russell E. McDuff, and William S. D. Wilcock. "Optical plume velocimetry: a new flow measurement technique for use in seafloor hydrothermal systems". *Exp Fluids*, 45:899–915, 2008.

[14] Crone, Timothy J. and Maya Tolstoy. "Magnitude of the 2010 Gulf of Mexico Oil Leak". *Science*, 330:Online, 2010.

[15] Farley, V., C. Belzile, M. Chamberland, J.-F. Legault, and K. R. Schwantes. "Development and testing of a hyperspectral imaging instrument for field spectroscopy". *Proceedings of SPIE*, 29–36. 2004.

[16] Gao, J. and M.B. Lythe. "The Maximum Cross-correlation approach to detecting translational motions from sequential remote-sensing images". *Computers and Geosciences*, 22(5):525–534, 1996.

[17] Gao, Jay and Matthew B. Lythe. "Effectiveness of the MCC Method in Detecting Oceanic Circulation Patterns at a Local Scale from Sequential AVHRR Images". *Photogrammetric Engineering and Remote Sensing*, 64:301–308, 1998.

[18] Hewett, T.A., J.A. Fay, and D.P. Hoult. *Atmospheric Environment*, volume 5. Pergamon Press, 1971.

[19] Hoult, D.P. and J.C. Weil. *Atmospheric Environment*, volume 6. Pergamon Press, 1972.

[20] Kerherve, F. and J. Fitzpatrick. "Measurement and analysis of the turbulent length scales in jet flows". *Experiments in Fluids*, Online first:Online first, 2010.

[21] Kurada, S., G. W. Rankin, and K. Sridhar. "Particle-imaging techniques for quantitative flow visualization: a review". *Optics and Laser Technology*, Vol 25:219–233, 1993.

[22] Lau, Jark C. and Philip J. Morris. *Journal of Fluid Mechanics*, volume 93, part 1. Cambridge University Press, 1979.

[23] List, E.J. *Annual Review of Fluid Mechanics*, volume 14. Annual Reviews Inc., 1982.

[24] Orfanidis, Sophocles J. *Optimum Signal Processing: An Introduction*. Macmillan, 1988.

[25] Papanicolaou, Panos N. and John E. List. "Investigations of round vertical turbulent buoyant jets". *Journal of Fluid Mechanics*, 195:341–391, 1988.

[26] Papoulis, Athanasios. *Signal Analysis*. McGraw-Hill, Inc, 1977.

[27] Pope, P.A. and W.J. Emery. "Sea Surface Velocities from Visible and Infrared Multispectral Atmospheric Mapping Sensor Imagery". *IEEE TRANSACTIONS ON GEOSCIENCE AND REMOTE SENSING*, 32:220–223, 1994.

[28] Sciences, Environmental and Clean Air Assistance Program Services Division. "Calculating Air Emissions for the Michigan Air Emissions Reporting System (MAERS)", January 2004. URL `http://www.deq.state.mi.us`.

[29] Subbarao, E.R. and B.J. Cantwell. "Investigation of a co-flowing buoyant jet: experiments on the effect of Reynolds number and Richardson number". *Journal of Fluid Mechanics*, 245:69–90, 1992.

[30] Tokmakian, Robin, P. Ted Strub, and Julie McClean-Padman. "Evaluation of the Maximum Cross-Correlation Method of Estimating Sea Surface Velocities from Sequential Satellite Images". *Journal of Atmospheric and Oceanic Technology*, 7:852–865, 1990.

[31] Various. *Infrared methods for gaseous measurements*, volume 7 of *Optical Engineering*. Marcel Decker, Inc., 1985.

[32] Weibring, P., M. Andersson, H. Edner, and S. Svanberg. "Remote monitoring of industrial emissions by combination of lidar and plume velocity measurements". *Applied Physics B: Lasers and Optics*, 66:383–388, 1998.

[33] Zukowska, D., A. Melikov, and Z. Popiolek. "Determination of the integral characteristics of an asymmetrical thermal plume from air speed/velocity and temperature measurements". *Experimental Thermal and Fluid Science*, In Press, Accepted Manuscript:tbd, 2010.

REPORT DOCUMENTATION PAGE

Form Approved
OMB No. 0704–0188

The public reporting burden for this collection of information is estimated to average 1 hour per response, including the time for reviewing instructions, searching existing data sources, gathering and maintaining the data needed, and completing and reviewing the collection of information. Send comments regarding this burden estimate or any other aspect of this collection of information, including suggestions for reducing this burden to Department of Defense, Washington Headquarters Services, Directorate for Information Operations and Reports (0704–0188), 1215 Jefferson Davis Highway, Suite 1204, Arlington, VA 22202–4302. Respondents should be aware that notwithstanding any other provision of law, no person shall be subject to any penalty for failing to comply with a collection of information if it does not display a currently valid OMB control number. **PLEASE DO NOT RETURN YOUR FORM TO THE ABOVE ADDRESS.**

1. REPORT DATE *(DD–MM–YYYY)*	2. REPORT TYPE	3. DATES COVERED *(From — To)*
24–03–2011	Master's Thesis	Aug 2009 — Mar 2011

4. TITLE AND SUBTITLE

Remote Quantification of Smokestack Total Effluent Mass Flow Rates Using Imaging Fourier-transfrom Spectroscopy

5a. CONTRACT NUMBER

5b. GRANT NUMBER

5c. PROGRAM ELEMENT NUMBER

6. AUTHOR(S)

Jacob L. Harley, Capt, USAF

5d. PROJECT NUMBER

5e. TASK NUMBER

5f. WORK UNIT NUMBER

7. PERFORMING ORGANIZATION NAME(S) AND ADDRESS(ES)

Air Force Institute of Technology
Graduate School of Engineering and Management (AFIT/EN)
2950 Hobson Way
WPAFB OH 45433-7765

8. PERFORMING ORGANIZATION REPORT NUMBER

AFIT/GE/ENP/11-M01

9. SPONSORING / MONITORING AGENCY NAME(S) AND ADDRESS(ES)

Intentionally Left Blank

10. SPONSOR/MONITOR'S ACRONYM(S)

11. SPONSOR/MONITOR'S REPORT NUMBER(S)

12. DISTRIBUTION / AVAILABILITY STATEMENT

APPROVED FOR PUBLIC RELEASE; DISTRIBUTION UNLIMITED.

13. SUPPLEMENTARY NOTES

14. ABSTRACT

A Telops Hyper-Cam midwave infrared $(1.5 - 5.5\,\mu m)$ imaging Fourier-transform spectrometer (IFTS) was used to estimate industrial smokestack total effluent mass flow rates by combining spectrally-determined species concentrations with flow rates estimated via analysis of sequential images in the raw interferogram cube. Strong emissions from H_2O, CO_2, CO, SO_2, and NO were observed in the spectrum. A previously established plume radiative transfer model was used to estimate gas concentrations, and a simple temporal cross-correlation analysis of sequential imagery enabled an estimation of the flow velocity. Final effluent mass flow rates for CO_2 and SO_2 of $13.5 \pm 3.78\,\mathrm{kg/s}$ and $71.3 \pm 19.3\,\mathrm{g/s}$ were in good agreement with *in situ* rates of $11.6 \pm 0.07\,\mathrm{kg/s}$ and $67.8 \pm 0.52\,\mathrm{g/s}$. NO was estimated at $16.1 \pm 4.19\,\mathrm{g/s}$, which did not compare well to the total NO_x $(NO + NO_2)$ reported value of $11.2 \pm 0.16\,\mathrm{g/s}$. Unmonitored H_2O, HCl, and CO were also estimated at $7.76 \pm 2.25\,\mathrm{kg/s}$, $7.40 \pm 2.00\,\mathrm{g/s}$, and $15.0 \pm 4.05\,\mathrm{g/s}$ respectively.

15. SUBJECT TERMS

Smokestack, FTS, IFTS, Pollutant, Turbulence, Fourier-transform, Imaging, Spectroscopy, Velocity estimation, Flow analysis

16. SECURITY CLASSIFICATION OF:			17. LIMITATION OF ABSTRACT	18. NUMBER OF PAGES	19a. NAME OF RESPONSIBLE PERSON
a. REPORT	b. ABSTRACT	c. THIS PAGE			Dr. Kevin C. Gross, AFIT/ENP
U	U	U	U	62	19b. TELEPHONE NUMBER *(include area code)* (937) 255-3636, x4558; kevin.gross@afit.edu

Standard Form 298 (Rev. 8–98)
Prescribed by ANSI Std. Z39.18